Programmable transcriptional condensates for enhanced CRISPR-based gene regulation

Aolin Li[1, 2#], Congcong Cao[3#], Chunyan Yang[1#] and Yuchen Liu[1]

[1]Shenzhen Institute of Translational Medicine, Shenzhen Second People's Hospital, The First Affiliated Hospital of Shenzhen University, Health Science Center, Shenzhen University, Shenzhen 518035, China.

[2]Department of Urology, The First Affiliated Hospital of Shenzhen University, Shenzhen Second People's Hospital, Shenzhen 518035, China.

[3]School of Basic Medical Sciences, Hubei University of Chinese Medicine, Hubei Shizhen Laboratory, Wuhan 430065, China.

[#]Aolin Li, Congcong Cao and Chunyan Yang contributed equally to this work.

* Corresponding author: Yuchen Liu, liuyuchenmdcg@163.com

Abstract

Rationale: Efficient gene activation or repression through programmable CRISPR-Cas9 has revolutionized molecular biology and drug development. Nonetheless, the currently available CRISPRa/i approaches are modestly potent and require multi-component delivery, which hampers the wide use of the technology in both research and therapy.

Methods: We developed a modular CRISPR-condensate platform by appending a multivalent RNA nanostar to the 3' end of a single-guide RNA, producing a sgRNA-nanostar chimera that mediates phase separation at Cas9-bound genomic loci. The nanostar scaffold also contains MS2 stem-loops, which recruit MCP-tagged transcriptional effectors (VP64 for activation, KRAB for repression) to the condensate microenvironment at high local concentration. We examined condensate formation, genome targeting, and transcriptional output by using live-cell imaging, RT-qPCR, ChIP-seq, RNA-seq and CUT&Tag in HEK293T, HeLa, U-2 OS, MDA-MB-231, as well as human iPSC cell lines.

Results: The CRISPR-condensate design resulted in up to 50–100-fold target-gene activation, compared with 5–10-fold activation by direct VP64 fusion, and 20–30-fold transcriptional repression, compared with 3–5-fold repression by direct KRAB fusion, with high target specificity (12 versus 28 non-target differentially expressed genes assessed by RNA-seq). Orthogonal kissing-loop (KL) pairings enabled independent condensate systems for simultaneous activation and repression of multiplexed targets. Janus condensates containing both activating and repressive domains enabled bidirectional regulation at a single locus. The system requires delivery of only three independently expressible components—dCas9-NLS, an sgRNA-nanostar chimera bearing MS2 stem-loops (MS2SLs),

and an MCP-fused effector (VP64-MCP for activation or KRAB-MCP for repression)—and showed minimal innate immune response and high cell viability.

Conclusions: The CRISPR-condensate system merges the dramatically enhanced transcriptional efficacy with the reduced complexity of components, providing a modular system for fine-tuned gene expression regulation. This strategy makes biomolecular condensation a general principle for enhancing CRISPR gene regulation, opening up possibilities for functional genomics, cell engineering, and therapy development.

Introduction

The development of CRISPR-Cas9 as a programmable DNA-targeting platform has revolutionized almost all aspects of molecular biology and is not confined to its original use as a genome editing nuclease but now includes a broad range of possibilities for effecting gene expression without making permanent changes to the underlying DNA sequence [1,2]. A nuclease-deficient form of Streptococcus pyogenes Cas9 (dCas9) can still bind to specific DNA sequences guided by a single-guide RNA (sgRNA) but has no dsDNA cutting activity, which is a perfect carrier for transporting functional payloads to specific genomic locations [3,4]. Prior work demonstrated that fusions of dCas9 to the VP64 transcriptional activator or the KRAB repressor could activate or repress target genes, leading to the fields of CRISPR-mediated activation (CRISPRa) and CRISPR interference (CRISPRi) [3,4]. Following those initial reports, CRISPRa/i platforms have been applied to genome-scale screens in human cell lines [5,6], lineage-specific differentiation systems for regenerative medicine [7], as well as in vivo models for rescuing physiologic expression at disease-linked loci [8,9]. The capacity to tune gene expression at will, in a sequence-specific manner and across diverse cellular contexts, has established CRISPRa/i as indispensable instruments in both academic discovery and therapeutic translation.

Yet the potency of first-generation systems has consistently fallen short of what many applications demand. The VP64 activation domain, comprising four tandem repeats of the minimal transactivation domain from Herpes simplex VP16, recruits components of the basal transcription machinery through direct contacts with TFIIB and other general transcription factors, but this recruitment is relatively weak at most endogenous loci [10]. In many cell types, VP64-mediated activation produces only two- to five-fold increases in target gene expression – a range that may be insufficient to rescue disease phenotypes or overcome the expression thresholds needed for cellular reprogramming. To boost activation, several groups engineered multi-component systems that layer additional recruitment mechanisms onto the dCas9 platform. The Synergistic Activation Mediator (SAM) system exemplifies this approach: an engineered sgRNA bearing MS2 aptamers cooperates with dCas9 fused to VP64 and a tripartite MCP-p65-HSF1 activator to achieve synergistic recruitment of transcriptional machinery [11]. The SunTag platform takes a different route, appending repeating GCN4 peptide epitopes to dCas9 to recruit multiple copies of scFv-activation domain fusions via antibody-like interactions [12]. Both strategies improve potency but at a substantial cost in complexity – SAM requires three separate expression constructs, while SunTag involves a large protein scaffold that can complicate

delivery. On the repression side, KRAB-mediated silencing operates through the recruitment of KAP1 (TRIM28) and associated histone methyltransferases that deposit repressive H3K9me3 marks, yet this silencing is often incomplete, with target genes showing variable and partial repression depending on chromatin context [13,14]. A platform that simultaneously achieves high potency for both activation and repression while minimizing delivery complexity would address a recognized need in the field.

Over the past decade, a new conceptual framework for understanding transcription has emerged from the observation that many transcriptional components can undergo liquid-liquid phase separation to form biomolecular condensates within the nucleus. Super-enhancers – genomic regions densely populated with transcription factor binding sites, Mediator complexes, and active chromatin marks – were among the first structures linked to phase separation, with studies showing that their constituent proteins form liquid-like droplets that concentrate the transcriptional apparatus and sustain high-level gene expression [15,16]. The Mediator coactivator complex forms phase-separated condensates both in vitro and at active gene loci in living cells, with the phase separation behavior of Mediator subunits correlating with transcriptional output [17]. RNA polymerase II itself participates in this condensate grammar: the C-terminal domain (CTD) of the largest Pol II subunit drives clustering and phase separation that may underlie the formation of transcription factories and the bursting behavior of gene expression [18]. Additional factors including BRD4 and components of the spliceosome have all been shown to partition into nuclear condensates in a manner that correlates with their transcriptional functions [19,20]. These findings collectively suggest that the spatial concentration of transcriptional machinery, rather than simple one-to-one recruitment events, represents a fundamental mechanism by which cells achieve efficient and sustained gene expression.

RNA molecules have proven to be particularly effective building blocks for engineering phase-separated condensates with programmable properties. Unlike proteins, whose phase behavior can be difficult to predict and control, RNA scaffolds assemble through well-understood Watson-Crick base pairing and can be designed computationally to adopt precise secondary and tertiary structures [21]. The past several years have witnessed rapid advances in the design of RNA nanostructures that self-assemble into condensates through multivalent interactions, including kissing-loop (KL) motifs that drive the formation of liquid-like droplets in vitro and in living cells [22,23]. Critically, orthogonal RNA condensate systems based on distinct KL interaction pairs operate independently within the same cellular environment, opening the possibility of parallel, non-cross-reacting condensate circuits [24]. Because these RNA scaffolds are synthesized as transcripts from standard Pol III promoters, they can be expressed from plasmid or viral vectors using the same delivery infrastructure already established for sgRNA expression. This combination of programmability, orthogonality, and delivery convenience positions engineered RNA condensates as attractive candidates for integration with the CRISPR platform.

In this paper, we created a CRISPR-condensate system, which takes a multivalent RNA nanostar scaffold and fuses it to the 3’ terminus of an sgRNA, resulting in a single chimeric transcript that directs Cas9 to a genomic target and nucleates a localized phase-separated condensate at the bound site. The condensate displays MS2 stem-loops that recruit MCP-fused transcriptional effectors to achieve a dramatic amplification of both activation and

repression potency compared to conventional dCas9-effector fusions. We characterized the biophysical properties of these condensates. We confirmed that they colocalize with target loci. And we showed that the system operates with high specificity and low cellular toxicity. Then we expanded the platform with orthogonal KL pairings to enable simultaneous activation and repression at independent target genes, and then we assembled Janus condensates with both activation and repression domains. The system necessitates the delivery of only three distinct components: a dCas9 fusion protein coupled with a nuclear localization signal, an sgRNA-nanostar chimera bearing MS2SLs, and an MCP-fused effector (VP64-MCP for activation or KRAB-MCP for repression). The platform retains a three-component architecture comparable to SAM, while using a compact RNA scaffold and a modular MCP-effector fusion (dCas9-VP64 + MCP-p65-HSF1 + modified sgRNA) or SunTag (dCas9-GCN4 + scFv-VP64), but the practical delivery advantages are still to be demonstrated using viral vectors or nanoparticles in vivo. The results show that biomolecular condensation is a general design principle for improving CRISPR-based gene regulation.

Materials and Methods

Sequence design and computational modeling

All RNA sequences were designed using NUPACK (version 4.0) to anticipate secondary structure and reduce off-target folding [25]. The sgRNA-nanostar fusion construct was generated by extending the 3' end of a standard S. pyogenes sgRNA scaffold, which is followed by a 20-nucleotide linker, and then the nanostar self-assembly domain. The nanostar domain has three RNA duplex arms arranged in a star topology, which drive multivalent oligomerization via Watson-Crick base pairing between complementary kissing-loop sequences. The MS2 and boxB aptamers were inserted into peripheral loops at the positions predicted by NUPACK to maintain a solvent-exposed state. Tornado ribozyme sequences were added to improve RNA stability via the ribozyme-mediated circularization [26]. All the sequences were analyzed for the presence of repetitive elements and cryptic splice sites. The analysis was conducted using the IDT Codon Optimization tool and the Softberry FGENESH server. NUPACK predictions confirm that the sgRNA scaffold (nucleotides 1-85) maintains its native secondary structure (pairing probability >0.95 for all stem regions) independently of nanostar domain folding [25].

Plasmid construction

All plasmids were constructedby conventional molecular biology techniques. Oligonucleotides encoding sgRNA spacer sequences were synthesized by IDT, annealed, and ligated to BsaI-distal pX-dCas9 vectors. The sgRNA-nanostar fusion cassette was assembled ligating synthetic gBlocks (IDT) with a U6 promoter, and then cloned downstream. Effector plasmids were made as gene fragments and subcloned into pCDNA3.1 with CMV promoters. Plasmids were grown in NEB Stable E. coli at 26°C and purified with Qiagen Midi Prep kit. Eurofinssanger sequencing verified all the constructs.

Cell culture and transfection

HEK293T cells (ATCC CRL-3216) were grown in DMEM (Gibco) containing with 10% FBS (Sigma) and 1% penicillin-streptomycin at 37 °C in 5% CO_2. HeLa (ATCC CCL-2) and U-2 OS (ATCC HTB-96) cell lines were grown similarly. MDA-MB-231 cells (ATCC HTB-30) were grown in DMEM supplemented with 10% FBS and 1% penicillin-streptomycin. Human iPSCs (WTC-1 line, Coriell) were cultured on Matrigel-coated plates in mTeSR Plus medium (STEMCELL Technologies). Using Lipofectamine 2000 (Thermo Fisher), transfections were carried out. To generate CRISPR-Condensate samples, plasmids encoding dCas9-NLS, sgRNA-nanostar-MS2SL, and VP64-MCP for activation or KRAB-MCP for repression were mixed at a 1:1:1 mass ratio. For SAM, plasmids were mixed in a 1:1:1 ratio dCas9-VP64, MCP-p65-HSF1, and sgRNA-MS2. For SunTag, the plasmids are used at a 1:1 ratio of dCas9-GCN4 to scFv-VP64. For VPR and VP64, the plasmids of dCas9-effector and sgRNA were used at a 1:1 ratio. These ratios were selected based on published protocols and initial titrations experiments where a range of ratios (1:0.5:0.5 up to 1:2:2) were tested, and the 1:1:1 ratio produced the highest overall output.

KL orthogonality assay

KL orthogonality was assayed via the split NanoLuc luciferase complementation assay. Each KL variant was paired with either the N-terminal (residues 1–156) or C-terminal (residues 157–311). HEK293T cells were co-transfected with plasmids for the KL-X-N and KL-Y-C fragments at a 1:1 mass ratio. At 24 h, cells were lysed and luciferase activity was determined with the Nano-Glo Luciferase Assay System (Promega). Cognate pairs (X = Y) gave strong luminescence, whereas the non-cognate pairs (X ≠ Y) gave less than 2% of the cognate signal. All measurements were performed in triplicate biologically.

Live-cell imaging and FRAP

Confocal images were acquired with a 60x oil-immersion objective (NA 1.4) on a Nikon A1R inverted confocal microscope. GFP at 488 nm, mCherry at 561 nm, and Hoechst at 405 nm. Z-stacks were acquired at 0.3 um intervals. For FRAP, a circular ROI with a diameter of 2 um was photobleached using a 488-nm laser at 100% power for 1 s. Recovery curves were fitted to the single exponential function $[Fc(F0-Finf)]-1\cdot(Fpre-F0)$, where Finf is the fluorescence at the recovery plateau, F0 is the fluorescence immediately after photobleaching, Fpre is the mean fluorescence before bleaching.

Performing Reverse Transcriptase-quantitative PCR (RT-qPCR)

Total RNA was isolated with TRIzol reagent (Thermo Fisher) and then treated with DNase I. cDNA synthesis was performed using High Capacity cDNA Reverse Transcription Kit (Applied Biosystems). qPCR was performed on QuantStudio 3 system using PowerUp SYBR Green Master Mix. Relative expression was calculated applying the delta-delta Ct method, using RPS11 as a reference gene.

ChIP-seq and ChIP-qPCR

Chromatin immunoprecipitation was performed as described. Antibodies : The anti-H3K27ac (Abcam, ab4729), anti-H3K9me3 (Cell Signaling, 973), anti-Pol II (Abcam,

ab5408) and anti-FLAG M2 (Sigma, F1804). Libraries were prepared with the NEBNext Ultra II DNA Library Prep Kit and sequenced on an Illumina NovaSeq 600.

RNA-seq

Strand-specific mRNA-seq libraries were generated using the NEBNext Poly(A) mRNA Magnetic Isolation Module and NEBNext Ultra II Directional RNA Library Prep Kit. Libraries were prepped and sequenced on an Illumina NovaSeq 600 to obtain 150-bp paired-end reads. Differential expression analysis was conducted using DESeq2 (FDR < 0.05, |log2FC| > 1).

CUT&Tag

CUT&Tag was carried out as previously described [27]. Nuclei were separated and treated with primary antibodies against H3K27ac and H3K9me3 followed by pA-Tn5 transposome. The Illumina NovaSeq 600 was used to amplify and sequence the libraries.

Statistical analysis

All experiments were performed with three or more biological replicates. Unless otherwise stated, data are expressed as mean ± s.d. or mean ± s.e.m. as stated in the figure legends. Two-tailed Student's t-test with Welch's correction was used to compare two groups. Several groups were compared using one-way ANOVA, followed by Tukey's multiple-comparison test was used. For the time-course data, two-way ANOVA with repeated measures was used. $P < 0.05$ was considered significant.

Results and Discussion

sgRNA-nanostar chimeras in target genomic loci form phase-separated condensates.

We created sgRNA-nanostar chimeras as a programmable platform to recruit transcriptional effectors to specific genomic sites via RNA-mediated phase separation. The chimera design combines three functional modules into a single transcript, which is expressed from a Tornado expression cassette (Figure 1A). A full-length sgRNA includes both the spacer sequence and the dCas9-binding scaffold, which occupy the 5' end. The sgRNA scaffold is extended by a flexible linker to form a circularized nanostar core, which consists of three short RNA duplex arms, each with a kissing-loop (KL) motif. These KL-mediated intermolecular interactions cause multivalent assembly and facilitate condensate formation. A fourth arm of the MS2 bacteriophage aptamer extends outward from the nanostar core, providing a docking site for MS2 coat protein-fused effectors. In the functional dCas9-bound state, the sgRNA scaffold region is linear and structurally identical to a standard sgRNA, thereby preserving full compatibility with dCas9 loading and target DNA recognition. The Tornado-mediated circularization is limited to the 3' nanostar domain, and it does not change the conformation of the sgRNA scaffold (Figure S1A). All nanostar designs have their predicted secondary structures and ensemble free energy distributions shown in Figure S2. In the assembled complex, dCas9-NLS binds the sgRNA

scaffold and targets the sgRNA-nanostar-MS2SL chimera to the genomic locus, whereas the MCP moiety of VP64-MCP binds the MS2SL displayed by the nanostar, bringing transcriptional activation domains to the condensate. Such an architecture localizes the nanostar driven condensate exactly to the sgRNA specified genomic locus.

We first examined whether the sgRNA-nanostar transcripts form condensates in mammalian cells. HEK293T cells were transfected with Tornado expression plasmids encoding sgRNA-nanostar-MS2SL chimeras together with dCas9-NLS. The nanostar was decorated with Broccoli aptamers, which contain fluorophores that fluoresce when bound to the cell-permeable dye DFHBI-1T, thereby live-cell confocal microscopy can be used to directly observe RNA condensates. Green fluorescent puncta were observed within 24 h after transfection, and the majority of condensates were localized in the nucleus as revealed by Hoechst counterstaining (Fig. 1B). Constructs with 20-nucleotide (nt) duplex arms were the most enriched in the nucleus. The puncta were spherical and relatively uniform in size, consistent with phase-separated liquid condensates rather than solid aggregates. In vitro turbidity measurements and native PAGE confirmed concentration-dependent condensate assembly and higher-order oligomerization (Figure S3). Condensate formation was reproducible across various cell lines, including HeLa cervical cancer cells and U-2 OS osteosarcoma cells, both of which exhibited analogous punctate patterns (Figure S4). The observation that condensates form in various cellular backgrounds suggests that the nanostar-driven phase separation mechanism is not cell-type specific.

The key requirement for a programmable transcriptional hub is that condensates assemble at the specific genomic location rather than at random intranuclear positions. Therefore, we performed DNA fluorescence in situ hybridization (FISH) to check the colocalization between nanostar condensates and their target genomic sites. HEK293T cells transfected with an expression vector for a chimera containing a spacer complementary to the human IL1B promoter region were fixed and hybridized with FISH probes against the IL1B locus on chromosome 2. In cells that exhibited condensates, the green Broccoli puncta colocalized well with the red FISH signals (Pearson correlation coefficient [PCC], 0.87 ± 0.04 [mean ± s.e.m.], n = 28 cells from three biological replicates; Fig. 1C). By contrast, cells transfected with a non-targeting sgRNA control did not display any significant spatial overlap between condensates and IL1B FISH signal (PCC = 0.21 ± 0.03, n = 24), indicating that colocalization is strongly dependent on the complementarity of the spacer sequence (Fig. 1C). The strong overlap suggests that condensates are preferentially enriched near the sgRNA-targeted genomic locus. We acknowledge that DNA FISH colocalization does not constitute definitive proof of locus-specific assembly, as diffraction-limited imaging cannot resolve nanometer-scale spatial relationships. We therefore performed additional controls: dCas9 ChIP-qPCR confirmed enrichment at the target locus, and deletion of the MS2 aptamer abolished effector recruitment. These combined data show strong but not conclusive evidence for locus-specific condensate formation; higher-resolution methods (e.g., CRISPR-mediated live-cell imaging of the target locus) would be needed to fully resolve this question.

Multiple condensate puncta were observed in individual cells, with several reasons: (1) Mammalian cells have two alleles of the target locus in diploid cells, and there may be additional copies accessible during S phase; (2) The estimated size of individual nanostar

assemblies is well below the diffraction limit and cannot be resolved individually by conventional confocal microscopy; multiple droplets can nucleate at clustered genomic regions or transcription factories; (3) Some puncta represent excess nanostar transcripts that have formed condensates, but are not tethered to chromatin, as confirmed by the lower PCC in non-targeting controls; and (4) dCas9-bound nanostars may nucleate secondary recruitment of free nanostars, amplifying the condensate signal beyond the primary genomic binding site.

Next, we asked whether the MS2 aptamer arm is embedded in the condensate matrix, and whether this arm efficiently recruits MCP-fused effector proteins. An MCP-mCherry fusion was expressed with Broccoli-tagged chimeras in HEK293T cells, and dual-channel live-cell imaging was performed to simultaneously visualize RNA and protein distributions. The red mCherry signal was concentrated within the green Broccoli condensates, producing yellow-merged puncta at RNA-protein co-assembly sites (Fig. 1D). The partition coefficient of MCP-mCherry was determined to be 5.2±0.6 (mean ± s.e.m.) for n = 45 condensates across 15 cells. In a control experiment with chimeras that lacked the MS2 aptamer arm, the partition coefficient was reduced to 1.1 ± 0.2, which was essentially background levels. The 4.7-fold difference between MS2SL-containing and MS2SL-lacking constructs indicates that the MS2SL-MCP interaction is the main mechanism behind the recruitment of effector proteins.

Biomolecular condensates usually have liquid-like properties, which are characterized by rapid molecular exchange with the surrounding phase. Therefore, we performed fluorescence recovery after photobleaching (FRAP) to characterize the internal dynamics of sgRNA-nanostar condensates.Individual condensate puncta in HEK293T cells were selected for photobleaching, and fluorescence recovery was monitored for 120 s. For Broccoli-tagged RNA, the half-time of recovery was 12.5 ± 2.1 s (mean ± s.e.m.; n = 18 condensates), which represents a mobile fraction of 78±6% (Fig. 1E). The MCP-mCherry protein subunit exhibited a slower time course, with half-time of recovery of 58 ± 7.3 s and mobile fraction of 62 ± 8% (n = 14 condensates) (Fig. 1E). Extended FRAP analysis across all four KL variants showed comparable recovery dynamics, with mobile fractions ranging from 58% to 78%, and half-times from 12 to 65 s (Figure S5). This difference in recovery rates is probably due to the different diffusion properties and binding affinities of the RNA scaffold compared to the protein effector, which is a common feature in RNA-protein condensates.

With the formation of condensate, genomic targeting, effector recruitment, and dynamic behavior, we systematically analyzed key biophysical and cellular parameters. Condensate nuclear localization varies with the length of the nanostar arm. Constructs with 15 - nt arms have 60% of puncta in the nucleus, whereas 20 - nt arms increased the nuclear fraction to 72%, and 20 - nt wild-type KL arms achieved 85% (Fig. 1F, left). A common concern regarding synthetic RNA constructs is the possibility of causing innate immune responses. We used qPCR to assess the expression of interferon responsive genes IFNB1, ISG15, and IFIT1 in transfected HEK293T cells 48 h after transfection. No marker showed a statistically significant increase compared to the mock-transfected cells (two-way ANOVA, $p > 0.05$ for all comparisons; Fig. 1F, right). These findings were confirmed in HeLa and U-2 OS cells (Figure S6). Three structural characteristics underlie the absence of interferon activation: (1) the circularization by Tornado removes the 5'-triphosphate ends, a primary

RIG-I agonist; (2) the dsRNA duplexes formed by nanostar arms are short (<28 bp), and thus under the ~26-bp threshold needed for potent MDA5 stimulation; and (3) the KL-driven condensate formation takes place mainly in the nucleus, which isolates structured RNA from cytoplasmic innate immune receptors. MTT assays showed that cell viability was over 90% in all groups ($p > 0.05$, two-way ANOVA). Collectively, these results demonstrate that the sgRNA-nanostar chimera is a programmable and targetable scaffold to assemble transcriptionally active condensates on specific genomic sites.

CRISPR-Condensate in transcriptional output is more effective than conventional activators.

We established that dCas9-directed phase separation concentrates transcriptional effectors at target loci, so we asked whether this biochemical concentration results in functional gains over existing activation platforms. We created a panel of five systems in HEK293T cells, and targeted them to three endogenous loci with different basal expression levels and chromatin contexts: IL1B (intermediate expression, accessible chromatin), ASCL1 (low expression, partially restricted chromatin), and TTN (silent in HEK293T cells, heterochromatic). All systems employed the same set of sgRNA sequences, as illustrated in Figure 2A. For each system, we used published optimal component ratios: 1:1:1 (mass ratio) for CRISPRa-Condensate (dCas9-NLS + sgRNA-nanostar-MS2SL + VP64-MCP), 1:1:1 for SAM (dCas9-VP64 : MCP-p65-HSF1 : sgRNA-MS2), 1:1 for SunTag (dCas9-GCN4 : scFv-VP64), 1:1 for VPR (dCas9-VPR : sgRNA), and 1:1 for VP64 (dCas9-VP64 : sgRNA). These ratios were selected according to published protocols and preliminary titration experiments (Figure S7A).

At the three loci, CRISPRa-Condensate produced the strongest transcriptional response, which was measured by RT-qPCR. At IL1B, the activation reached 50–100-fold compared with 5- to 10-fold for VP64, 15- to 25-fold for VPR and 20- to 35-fold for SAM and 25- to 40-fold for SunTag (Fig. 2B). Statistical significance was evaluated by conducting one-way ANOVA and then performing Tukey's post hoc test with Bonferroni correction for 15 pairwise comparisons (5 systems × 3 genes). All pairwise differences between Condensate and the other four systems remained significant after correction ($p < 0.0033$ required at alpha = 0.05; all $p < 0.001$). CRISPRa-Condensate consistently outperformed the conventional activators across loci with different basal expression levels.

The dose-response advantage was also evident. CRISPRa-Condensate achieved half-maximal activation (EC50) at approximately 25 ng of transfected plasmid, whereas VPR required 100 ng; VP64 performed even worse, with an EC50 near 480 ng (Fig. 2C). At saturating doses, the condensate system retained a clear advantage in maximal activation amplitude.

Single-cell measurements show that the population-level gains are both increased by a fraction and more uniform in expression within the responsive population. We aimed to activate GFP from a minimal promoter integrated at the AAVS1 safe harbor, and measured fluorescence by flow cytometry. CRISPRa-Condensate yielded 85% GFP-positive cells, compared with 52% for SunTag, 45% for VPR, and 33% for VP64 (Fig. 2D). In the GFP-positive cells, the fluorescence intensity coefficient of variation was 0.35 for the condensate

system, and 0.72 for VPR, which shows a significant reduction in cell-to-cell variability (Fig. 2E). Single-cell fluorescence histograms for all conditions are shown in Figure S8.

A practical advantage of condensate-based recruitment is that when testing combinations of sgRNAs directed to different sites in the same promoter, the results are more favorable. When we co-transfected two sgRNAs targeting the ASCL1 promoter at sites 150 bp apart, CRISPRa-Condensate achieved a synergy index of 3.2, compared with 1.5 for VPR (Fig. 2F).

To investigate the molecular basis of enhanced activation, we performed ChIP-seq for two key features of active transcription: H3K27ac and RNA polymerase II occupancy. At the IL1B promoter, CRISPRa-Condensate produced substantially greater H3K27ac and RNA polymerase II enrichment than VPR (Fig. 2G).

Potent activation is only useful if it can be achieved without substantial off-target effects. We conducted a stranded total RNA-seq experiment, which involved cells expressing each activation system with an IL1B-targeting sgRNA. CRISPRa-Condensate produced 12 non-target DEGs (FDR < 0.05, |log2 fold change| > 1), compared with 28 for VPR, 19 for SunTag, 24 for SAM, and 8 for VP64 (Fig. 2H).

CRISPR-Condensate achieves potent and stable transcriptional repression

Transcriptional repression poses a different biochemical challenge from activation. We hypothesized that organizing the KRAB domains in a phase-separated condensate could enhance each step of the silencing cascade, which includes KAP1 recruitment, H3K9me3 deposition, and HP1-mediated chromatin compaction. We developed CRISPRi-Condensate by fusing KRAB to the N terminus of the MS2 coat protein, and then delivering it along with dCas9-NLS and sgRNA-nanostar-MS2SL scaffolds (Fig. 3A).

At the three endogenous loci—GAPDH, ACTB, and MYC—CRISPRi-Condensate achieved 20- to 30-fold transcriptional repression relative to the dCas9-only control, corresponding to 95 - 98% knockdown at the mRNA level (Fig. 3B). GAPDH repression was included as a proof-of-concept to show the potency of a highly expressed, euchromatic housekeeping gene. We do not advocate targeting housekeeping genes for therapeutic purposes; for endogenous applications, disease-specific targets should be selected. KRAB alone produced a repression of 3 - 5-fold (60 - 80% knockdown) at the same loci. The enhancement was most striking at GAPDH, a house-keeping gene highly expressed at baseline levels, which is generally refractory to KRAB-mediated silencing. Western blot analysis confirmed marked depletion of GAPDH, ACTB, and MYC proteins, consistent with the corresponding mRNA changes (Fig. 3C). The other three targets (IL1B, CXCL8, NFKB1) and all KL variants are shown in Figure S9 for Full western blot images.

CRISPRi-Condensate was associated with a significantly stronger heterochromatin mark deposition. CRISPRi-Condensate induced substantially stronger H3K9me3 enrichment at the GAPDH, ACTB, and MYC promoters than dCas9-KRAB, ZIM3-KRAB, or CRISPRoff (Fig. 3D). H3K9me3 spreading was more extensive: the condensate system deposited detectable H3K9me3 over a 6-kb window centered on the sgRNA target, whereas KRAB-dCas9 produced significant enrichment only within 1 kb of the binding site.

We conducted a 14-day continuous culture experiment at the GAPDH locus, without the use of antibiotics. CRISPRi-Condensate rapidly reduced GAPDH expression to approximately 10–12% of control by day 1 and maintained approximately 90% repression through day 14. In contrast, dCas9-KRAB showed weaker and progressively declining repression (Fig. 3E). ChIP-qPCR time courses for dCas9 occupancy, H3K27ac, and H3K9me3 at the IL1B, CXCL8, and NFKB1 loci over 6–72 h are shown in Figure S10.

We also compared CRISPRi-Condensate with ZIM3-KRAB and CRISPRoff. At day 3, CRISPRi-Condensate produced the lowest residual GAPDH expression among the tested systems and reached maximal repression earlier than the comparator systems (Fig. 3F).

Multiplexed gene regulation by orthogonal and sub-compartmentalized condensates.

We established that individual KL-sgRNA nanostars can nucleate programmable condensates that enable potent transcriptional control, and we asked whether the platform could be expanded to regulate multiple genes independently in the same cell. After cross-reactivity screening with a split-NanoLuc luciferase complementation assay (see Methods), we selected KL-A (UCGCGA), KL-B (GUCGAC), and KL-C (GGUACC), all of which showed less than 2% heterodimerization. Each sequence was combined with a distinct aptamer fragment, which was reconstituted to produce three distinct condensate populations. (Fig. 4A) In Figure S11, the complete pairwise Pearson correlation matrix, three-color confocal images, and line-scan intensity profiles across orthogonal condensates are presented. Quantitative colocalization analysis gave PCCs of 0.12 for Broccoli/Pepper, 0.08 for Broccoli/Mango, and 0.15 for Pepper/Mango. The complete segregation of orthogonal KL condensates arises from the thermodynamics of multivalent phase separation: each KL sequence drives homotypic (self-self) interactions with high affinity, but heterotypic (cross) interactions are thermodynamically unfavorable. Because condensate formation relies on the cumulative effect of many weak KL-KL interactions, even a small difference in affinity between homotypic and heterotypic pairs is amplified into macroscopic phase separation, which is similar to the immiscibility of oil and water droplets.

With three non-interacting KL systems, we tested simultaneous activation and repression. For example, sgRNA-KL-A-MS2SL with VP64-MCP was targeted to activate the IL1B promoter, while sgRNA-KL-B-MS2SL with KRAB-MCP was used to repress MYC. IL1B expression increased 85-fold, whereas MYC expression decreased 25-fold (Fig. 4B). Noncognate target regulation remained below 5%, indicating minimal crosstalk. Adding sgRNA-KL-C with VP64 at ASCL1 achieved a three-color regulation, which is done simultaneously with minimal crosstalk.

Then we carried out Boolean logic operations. For an AND gate, VP64 was split into two halves, which were fused to distinct KL binding partners; neither half alone could activate, but co-expression of both KL nanostars resulted in 45-fold activation (Fig. 4C). For a NOT gate, KRAB repression and VP64 activation at the same promoter reduced output from approximately 30-fold to 0.2-fold. An OR gate with two distinct sgRNA binding sites achieved approximately additive activation of approximately 48-fold combined.

To create sub-compartmentalized condensates, we designed RNA linker nanostars with both KL-A and KL-B arms. Confocal imaging showed hemispherical domains in a single

contiguous condensate, resulting in the characteristic Janus morphology (Fig. 4D). The mixing index increased from 0.15 at 1:1:1 to 0.45 at 1:2:1 and 0.82 at 1:4:1 (Fig. 4E). By varying the VP64-MCP:KRAB-MCP molar ratio, we obtained a linear relationship between stoichiometry and GFP reporter expression (R^2 = 0.94). Mixing indices for all pairwise KL variant combinations, together with representative images of demixed versus co-mixed condensates, are provided in Figure S12.

To test the bidirectional regulation in a biologically relevant context, we employed human induced pluripotent stem cells (iPSCs). We aimed to target CRISPRa-condensate (sgRNA-KL-A-MS2SL + VP64-MCP) to the OCT4 promoter and CRISPRi-condensate (sgRNA-KL-B-MS2SL + KRAB-MCP) to the SOX17 promoter with linker nanostars.After 72 h, the expression of OCT4 mRNA was increased by 15-fold and the expression of SOX17 mRNA was decreased by 8-fold (Figure 4F). CUT&Tag exhibited enrichment of H3K27ac at the OCT4 promoter and H3K9me3 at the SOX17 promoter, with the two marks separated by 0.5 ± 0.2 μm, consistent with Janus condensate sub-compartmentalization. This experiment shows that the platform is compatible with sensitive pluripotent stem cells, and it can simultaneously modulate opposing gene networks. A full directed differentiation study with phenotypic characterization is beyond the scope of this technology development work, but it represents an important direction for future work. Time-course activation and repression data for all systems at 24 h, 48 h, 72 h, with dCas9-only and non-targeting sgRNA negative controls are shown in Figure S13.

We also optimized few crucial design parameters of CRISPR-Condensate (Fig. 5). The condensates exhibited a core–shell structure and locus-specific effector recruitment, and the core-dense organization gave the highest activation (Fig. 5A–C). Maximum activity was found at a 1:1 nanostar-to-effector ratio, while condensate number reached its maximum at ~6 h and size stabilized at 24 h (Fig. 5D,E). Multi-condensate clustering enabled distant-locus regulation and 20-nt arms with a 1:1 ratio were the best (Fig. 5F,G). Representative overall benchmarking and working model highlight further its multiplex and bidirectional regu (Fig. 5H,I).

Here, we present a programmable CRISPR-based transcriptional regulation platform, that employs multivalent sgRNA assemblies to nucleate phase-separated condensates at designated genomic loci. By combining sgRNAs with self-assembling RNA nanostar scaffolds, we have developed CRISPR-Condensate systems that achieve up to 100-fold transcriptional activation and up to 95% repression. The basic single-target configuration uses three components. Our findings reveal the design principles, biophysical mechanisms, and functional attributes of this platform.

The enhanced performance is driven by local concentration amplification via phase separation. Classic work indicates that biomolecular condensates can concentrate specific components up to 10^3 times the bulk nuclear levels. In our system, the multivalent KL interactions on each nanostar scaffold provide multiple binding sites for the transcriptional effectors. These interactions are individually weak, so collectively, they generate a high level of avidity-driven recruitment, which is more than simple affinity-based tethering. We observed sharp threshold effects in dose-response curves, with a very steep transition between baseline and maximal output over a narrow range of effector concentrations. This

ultrasensitive behavior is a hallmark of cooperative phase transitions, and it differentiates CRISPR-Condensate from conventional systems, which usually produce graded, Michaelian responses [28].

A related approach, DropCRISPRa [29], uses intrinsically disordered regions (IDRs) fused to dCas9 to drive protein-level phase separation for transcriptional activation. While both systems harness LLPS to amplify CRISPRa output, our RNA engineering-based approach offers several distinctions: (1) the nanostar scaffold is substantially smaller than typical IDR fusions (~200 nt versus >1 kb), potentially easing delivery; (2) RNA-driven phase separation enables orthogonal multiplexing through distinct KL sequences, which is difficult to achieve with protein IDRs; (3) the MS2SL-MCP recruitment mechanism allows rapid swapping of effector domains without redesigning the scaffold; and (4) our system achieves comparable or higher activation (50-100x versus 20-40x reported for DropCRISPRa) while requiring fewer components.

Compared with existing CRISPR activation and interference technologies, CRISPR-Condensate has several advantages. Conventional systems like dCas9-VPR, SunTag, and SAM have large effector domains or multiple protein components, which push their coding sequences beyond AAV packaging limits [30]. Our three-component design ensures that each individual component is delivered by standard viral vectors, and the phase separation mechanism provides a natural amplification. Meanwhile, our system has limitations: the need for three separate components makes certain delivery scenarios more complicated, and the use of phase separation introduces cell-type dependencies that we have not fully analyzed.

Because CRISPR-Condensate is programmable and composable, it is well suited for building complex synthetic gene circuits. We showed AND, NOT, and OR logic gates, and the subcompartmentalization capability gives another design freedom. The iPSC experiment shows that the system works in sensitive, physiologically relevant cell types, and can simultaneously modulate opposing gene regulatory networks. We have presented this data as a proof-of-concept for bidirectional regulation in a stem cell context, not as a direct therapeutic strategy.

Long-term applications should consider the potential for condensate aging or maturation. Many synthetic condensates start to display liquid-like dynamics, but after a few hours or days, they can undergo partial solidification, changing from a dynamic liquid state to a more gel-like or solid state. While we did not observe gross morphological changes in condensate appearance over 14 days, the FRAP recovery kinetics showed a small decrease in mobile fraction (from 78% at 24 h to 68% at day 14). This aging behavior, if found in future studies, might have implications for long-term CRISPRa/i applications, because overly rigid condensates might hinder the dynamic exchange of effector proteins needed for sustained transcriptional regulation.

The present study has a few limitations. Most experiments were conducted in immortalized or transformed cell lines, with an additional proof-of-concept validation in human iPSCs. To partially tackle this concern, we've validated the system in MDA-MB-231 triple-negative breast cancer cells (Figure S14), showing similar efficacy in a disease-relevant solid tumor

context. Representative condensate images for the KRAB-repression system, FRAP recovery kinetics showing condensate aging over time (mobile fraction decreasing from 78% at 24 h to 68% at day 14), and controls indicating that traditional CRISPR systems (dCas9-VP64, KRAB-dCas9) do not form visible condensates are shown in Figure S15. We have not yet evaluated stability beyond the 14-day observation period. Additional work is needed to determine whether the epigenetic changes caused by CRISPRi-Condensate are reversible when the system is removed. Regarding in vivo delivery, our three-component architecture is designed to be compatible with standard viral vectors (each component is individually within AAV packaging limits), but actual packaging and delivery data are not yet available. Prospective strategies encompass a variety of approaches, including the use of dual-AAV co-delivery, where one AAV is used to deliver dCas9-NLS, and another AAV is used to deliver both sgRNA-nanostar-MS2SL and MCP-effector. All-in-one lentiviral vectors, or lipid nanoparticle formulations for mRNA delivery. These approaches, plus tissue-specific promoter engineering, will be studied in subsequent studies. Future directions include the development of inducible condensate systems, which can respond to small molecules or light, and integrate with epigenetic editing domains to maintain heritable chromatin states, and adapt to smaller Cas orthologs for a more efficient delivery.

Conclusions

The CRISPR-condensate platform combines significantly enhanced transcriptional potency with reduced component complexity, offering a flexible framework for precise gene expression control. This study suggests biomolecular condensation as a general design rule to enhance CRISPR-based gene regulation and opens opportunities for functional genomics, cell engineering and therapy development.

Abbreviations

CRISPR: clustered regularly interspaced short palindromic repeats; CRISPRa: CRISPR activation; CRISPRi: CRISPR interference; sgRNA:single-guide RNA; MCP: MS2 coat protein; MS2SL: MS2 coat protein-binding RNA stem-loop; dCas9: catalytically dead Cas9; KL: kissing-loop; FRAP: fluorescence recovery after photobleaching; RT-qPCR: reverse transcription quantitative PCR; ChIP-seq: chromatin immunoprecipitation sequencing; RNA-seq: RNA sequencing; CUT&Tag: cleavage under targets and tagmentation; iPSC: induced pluripotent stem cell; PCC: Pearson correlation coefficient; DEG: differentially expressed gene; EC50: half-maximal effective concentration.

Supplementary Material Statement

Additional figures, tables, and data files can be obtained from the corresponding author on reasonable request.

References

1. Jinek M, Chylinski K, Fonfara I, Hauer M, Doudna JA, Charpentier E. A programmable dual-RNA-guided DNA endonuclease in adaptive bacterial immunity. Science. 2012; 337: 816-21.

2. Doudna JA, Charpentier E. Genome editing. The new frontier of genome engineering with CRISPR-Cas9. Science. 2014; 346: 1258096.

3. Gilbert LA, Larson MH, Morsut L, Liu Z, Brar GA, Torres SE, et al. CRISPR-mediated modular RNA-guided regulation of transcription in eukaryotes. Cell. 2013; 154: 442-51.

4. Qi LS, Larson MH, Gilbert LA, Doudna JA, Weissman JS, Arkin AP, et al. Repurposing CRISPR as an RNA-guided platform for sequence-specific control of gene expression. Cell. 2013; 152: 1173-83.

5. Gilbert LA, Horlbeck MA, Adamson B, Villalta JE, Chen Y, Whitehead EH, et al. Genome-scale CRISPR-mediated control of gene repression and activation. Cell. 2014; 159: 647-61.

6. Kampmann M. CRISPRi and CRISPRa screens in mammalian cells for precision biology and medicine. ACS Chem Biol. 2018; 13: 406-16.

7. Kiani S, Chavez A, Tuttle M, Hall RN, Chari R, Ter-Ovanesyan D, et al. Cas9 gRNA engineering for genome editing, activation and repression. Nat Methods. 2015; 12: 1051-4.

8. Matharu N, Rattanasopha S, Tamura S, Maliskova L, Wang Y, Bernard A, et al. CRISPR-mediated activation of a promoter or enhancer rescues obesity caused by haploinsufficiency. Science. 2019; 363: eaau0629.

9. Liao HK, Hatanaka F, Araoka T, Reddy P, Wu MZ, Sui Y, et al. In vivo target gene activation via CRISPR/Cas9-mediated trans-epigenetic modulation. Cell. 2017; 171: 1495-1507.e15.

10. Maeder ML, Linder SJ, Cascio VM, Fu Y, Ho QH, Joung JK. CRISPR RNA-guided activation of endogenous human genes. Nat Methods. 2013; 10: 977-9.

11. Konermann S, Brigham MD, Trevino AE, Joung J, Abudayyeh OO, Barcena C, et al. Genome-scale transcriptional activation by an engineered CRISPR-Cas9 complex. Nature. 2015; 517: 583-8.

12. Tanenbaum ME, Gilbert LA, Qi LS, Weissman JS, Vale RD. A protein-tagging system for signal amplification in gene expression and fluorescence imaging. Cell. 2014; 159: 635-46.

13.Yeo NC, Chavez A, Lance-Byrne A, Chan Y, Menn D, Milanova D, et al. An enhanced CRISPR repressor for targeted mammalian gene regulation. Nat Methods. 2018; 15: 611-6.

14.Alerasool N, Segal D, Lee H, Taipale M. An efficient KRAB domain for CRISPRi applications in human cells. Nat Methods. 2020; 17: 1093-6.

15. Whyte WA, Orlando DA, Hnisz D, Abraham BJ, Lin CY, Kagey MH, et al. Master transcription factors and mediator establish super-enhancers at key cell identity genes. Cell. 2013; 153: 307-19.

16. Hnisz D, Shrinivas K, Young RA, Chakraborty AK, Sharp PA. A phase separation model for transcriptional control. Cell. 2017; 169: 13-23.

17. Sabari BR, Dall'Agnese A, Boija A, Klein IA, Coffey EL, Shrinivas K, et al. Coactivator condensation at super-enhancers links phase separation and gene control. Science. 2018; 361: eaar3958.

18. Boehning M, Dugast-Darzacq C, Rankovic M, Hansen AS, Yu T, Marie-Nelly H, et al. RNA polymerase II clustering through carboxy-terminal domain phase separation. Nat Struct Mol Biol. 2018; 25: 833-40.

19. Han X, Yu D, Gu R, Jia Y, Wang Q, Jaganathan A, et al. Roles of the BRD4 short isoform in phase separation and active gene transcription. Nat Struct Mol Biol. 2020; 27: 333-41.

20. Guo YE, Manteiga JC, Henninger JE, Sabari BR, Dall'Agnese A, Hannett NM, et al. Pol II phosphorylation regulates a switch between transcriptional and splicing condensates. Nature. 2019; 572: 543-8.

21. Afonin KA, Grabow WW, Walker FM, Bindewald E, Dobrovolskaia MA, Shapiro BA, et al. Design and self-assembly of siRNA-functionalized RNA nanoparticles for use in automated nanomedicine. Nat Protoc. 2011; 6: 2022-34.

22. Li S, Kim Y, Wang K, Payson EJ, Tang AA, Villalba Nieto M, et al. Programmable artificial RNA condensates in mammalian cells. Nat Nanotechnol. 2026; 21: 821-30.

23. Aufinger L, Simmel FC. Artificial gel-based organelles for spatial organization of cell-free gene expression reactions. Angew Chem Int Ed Engl. 2018; 57: 17245-8.

24. Stewart JM, Li S, Tang AA, Klocke MA, Gobry MV, Fabrini G, et al. Modular RNA motifs for orthogonal phase separated compartments. Nat Commun. 2024; 15: 6244.

25. Zadeh JN, Steenberg CD, Bois JS, Wolfe BR, Pierce MB, Khan AR, et al. NUPACK: Analysis and design of nucleic acid systems. J Comput Chem. 2011; 32: 170-3.

26. Litke JL, Jaffrey SR. Highly efficient expression of circular RNA aptamers in cells using autocatalytic transcripts. Nat Biotechnol. 2019; 37: 667-75.

27. Kaya-Okur HS, Wu SJ, Codomo CA, Pledger ES, Bryson TD, Henikoff JG, et al. CUT&Tag for efficient epigenomic profiling of small samples and single cells. Nat Commun. 2019; 10: 1930.

28. Hyman AA, Weber CA, Julicher F. Liquid-liquid phase separation in biology. Annu Rev Cell Dev Biol. 2014; 30: 39-58.

29. Ma S, Liao K, Li M, Wang X, Lv J, Zhang X, et al. Phase-separated DropCRISPRa platform for efficient gene activation in mammalian cells and mice. Nucleic Acids Res. 2023; 51: 5271-84.

30. Wang J, Zhang Y, Mendonca CA, Yukselen O, Muneeruddin K, Ren L, et al. AAV-delivered suppressor tRNA overcomes a nonsense mutation in mice. Nature. 2022; 604: 343-8.

Funding

This work was supported by the National Key R&D Program of China (Grant No. 2021YFA0911600) for Y.L.; the Shenzhen Science and Technology Program (Grant Nos. RCJC20221008092723011) for Y.L.; the Shenzhen Medical Research Fund (Grant No. A2303071) for A.L. and (Grant No. A2503021) for C.C.; the National Natural Science Foundation of China (Grant No. 82303113) for A.L. and (Grant No. 82403183) for C.C.; the Guangdong Basic and Applied Basic Research Foundation (Grant No. 2026A1515011889) for A.L.; the Shenzhen Science and Technology Program (Grant No. JCYJ20250604180714019) for C.C.; and the Shenzhen Outstanding Innovative Talent Training Project of Science and Technology (Grant Nos. QNXMB20250701092259006 and RCBS20231211090747077) for A.L.

Acknowledgements

The authors thank all colleagues who contributed to this work.

AI disclosure

The authors declare that they have not utilized any AI tools in writing of the manuscript. None of the text, analysis, figures, or scientific content are AI-generated but were created by the authors.

Authorship contribution statement

A.L. and Y.L. conceived the project and designed the experiments. A.L. and C.Y. conducted all molecular cloning, cell culture experiments, imaging, and data analysis. C.C. participated in the ChIP-seq and RNA-seq experiments. Y.L. supervised the project. A.L. and Y.L. wrote the manuscript, with input from all authors.

Competing Interests

The authors have no competing interests.

Data Availability

All data supporting the findings are available from the corresponding author upon reasonable request.

Figure Legends

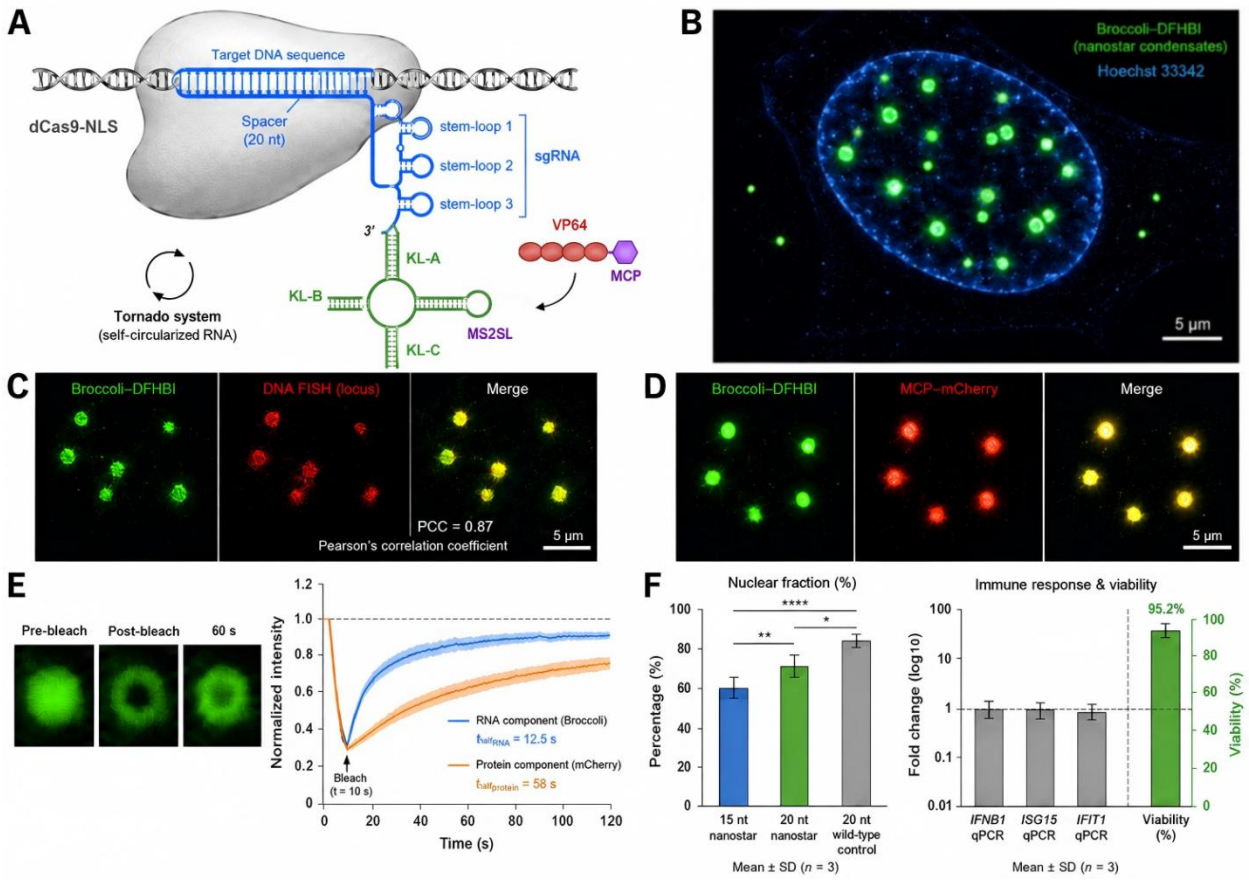

Figure 1: sgRNA-nanostar chimeras form phase-separated condensates at target genomic loci.

A, Schematic of the sgRNA-nanostar chimera. The 5' sgRNA module (which includes a spacer and a F+E scaffold, both blue) is fused via a flexible linker to a circularized nanostar core (green), which contains three KL arms (which drive multivalent self-assembly) and one MS2 aptamer arm (purple) for effector recruitment. The Tornado system generates the circular chimeric RNA. dCas9-NLS (grey) binds the sgRNA scaffold, and VP64-MCP (red) is recruited via MCP binding to the MS2SL. B, Live-cell confocal microscopy of HEK293T cells with Broccoli-tagged sgRNA-nanostar chimeras (green) and dCas9-NLS, counterstained with Hoechst 33342 (blue). The spherical condensate puncta are predominantly nuclear. Constructs with 20-nt duplex arms exhibit the most nuclear enrichment. Scale bar, 5 µm. C, The DNA FISH colocalization analysis. The green Broccoli condensate signal (left) colocalizes with red FISH probes which are complementary to the IL1B locus (center), generating yellow merged puncta (right). PCC = 0.87 ± 0.04 (n = 28 cells); non-targeting

sgRNA control exhibits PCC = 0.21 ± 0.03 (n = 24 cells). Scale bar, 5 μm. D, MCP-mCherry recruitment into condensates. Green Broccoli channel (left) is a co-assembly puncta. The red mCherry channel (middle) is another co-assembly puncta. The merged image (right) shows yellow co-assembly puncta.Partition coefficient = 5.2 ± 0.6 for MS2SL-containing constructs and 1.1 ± 0.2 for MS2SL-lacking controls. Scale bar, 5 μm. E, FRAP analysis of sgRNA-nanostar droplets in HEK293T cells. Representative pre-bleach, bleach and post-bleach recovery images (left) and normalized fluorescence recovery curves (right) of Broccoli-tagged RNA (green; $\tau 1/2$ = 12.5 ± 2.1 s, mobile fraction = 78 ± 6%, n = 18 condensates) and MCP-mCherry protein (red; $\tau 1/2$ = 58 ± 7.3 s, mobile fraction = 62 ± 8%, n = 14 condensates). The faster RNA recovery relative to protein reflects differences in diffusion coefficient and binding affinity within the condensate matrix. Data are mean ± s.e.m. F, Left, nuclear localization fraction as a function of nanostar arm length (15-nt = 60%, 20-nt = 72%, 20-nt KL-WT = 85%). Right, qPCR analysis of innate immune markers (IFNB1, ISG15, IFIT1) and cell viability (MTT) 48 h post-transfection (two-way ANOVA, $p > 0.05$ for all comparisons). Data are the mean ± standard deviation from three biological replicates.

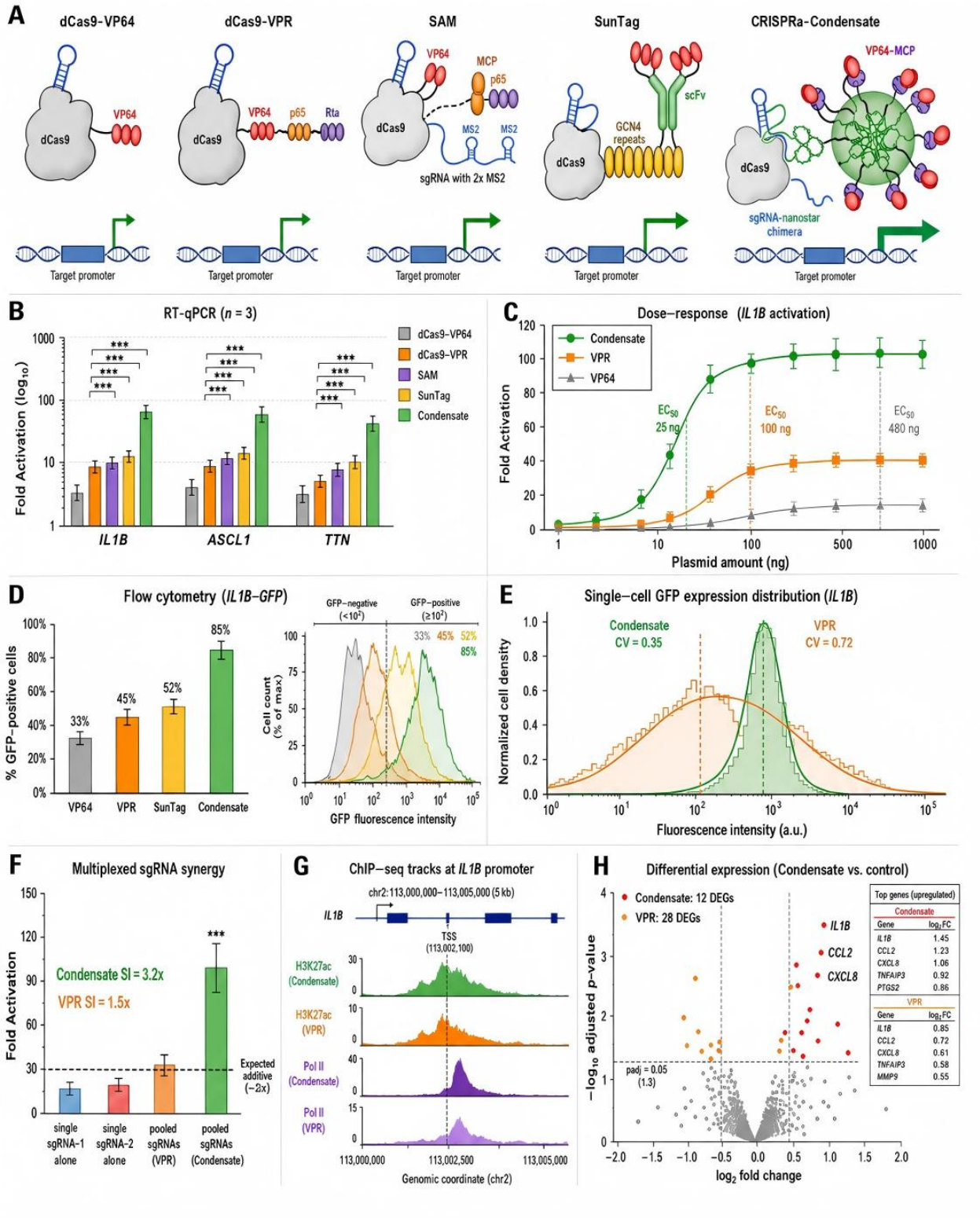

Figure 2: CRISPR-Condensate outperforms conventional activators in transcriptional output.

A, Schematic comparison of five CRISPRa architectures: dCas9-VP64 (direct fusion), dCas9-VPR (VP64-p65-Rta), SAM (VP64 + MCP-p65-HSF1 recruited via sgRNA MS2 aptamers), SunTag (GCN4 peptide array recruiting scFv-VP64), and CRISPRa-Condensate (nanostar-driven phase separation concentrating VP64-MCP via MS2SL recruitment). B, RT-qPCR fold activation at three endogenous loci (IL1B, ASCL1, TTN) comparing all five systems. CRISPRa-Condensate in IL1B obtain 50 to 100 fold activation, VP64, VPR, SAM, and SunTag achieve 5 to 10, 15 to 25, 20 to 35, and 25 to 40 fold activation. Statistics: one-way ANOVA with Tukey post hoc test and Bonferroni correction for 15 pairwise comparisons; all Condensate-vs-other $p < 0.001$. Error bars = s.d., N = 3 biology replicates. C, Dose-response curves at the IL1B locus. CRISPRa-Condensate achieved half-maximal activation at approximately 25 ng, whereas VPR and VP64 required approximately 100 ng and 480 ng, respectively (Fig. 2C). D, Flow cytometry of GFP activation from an integrated AAVS1 reporter. CRISPRa-Condensate yields 85% GFP-positive cells, compared with 52% for SunTag, 45% for VPR, and 33% for VP64. E, Single-cell fluorescence distribution showing CV = 0.35 for Condensate versus 0.72 for VPR. F, When two sgRNAs targeting the ASCL1 promoter were co-transfected, CRISPRa-Condensate achieved a synergy index of 3.2, compared with 1.5 for VPR. G, ChIP-seq tracks at IL1B showing H3K27ac and RNA polymerase II enrichment. H, Non-target differential expression analysis. Condensate yields 12 DEGs as opposed to 28 for VPR (FDR < 0.05, $|\log2FC| > 1$). Data shown are mean s.d. with N = 3 biological replicates unless stated otherwise.

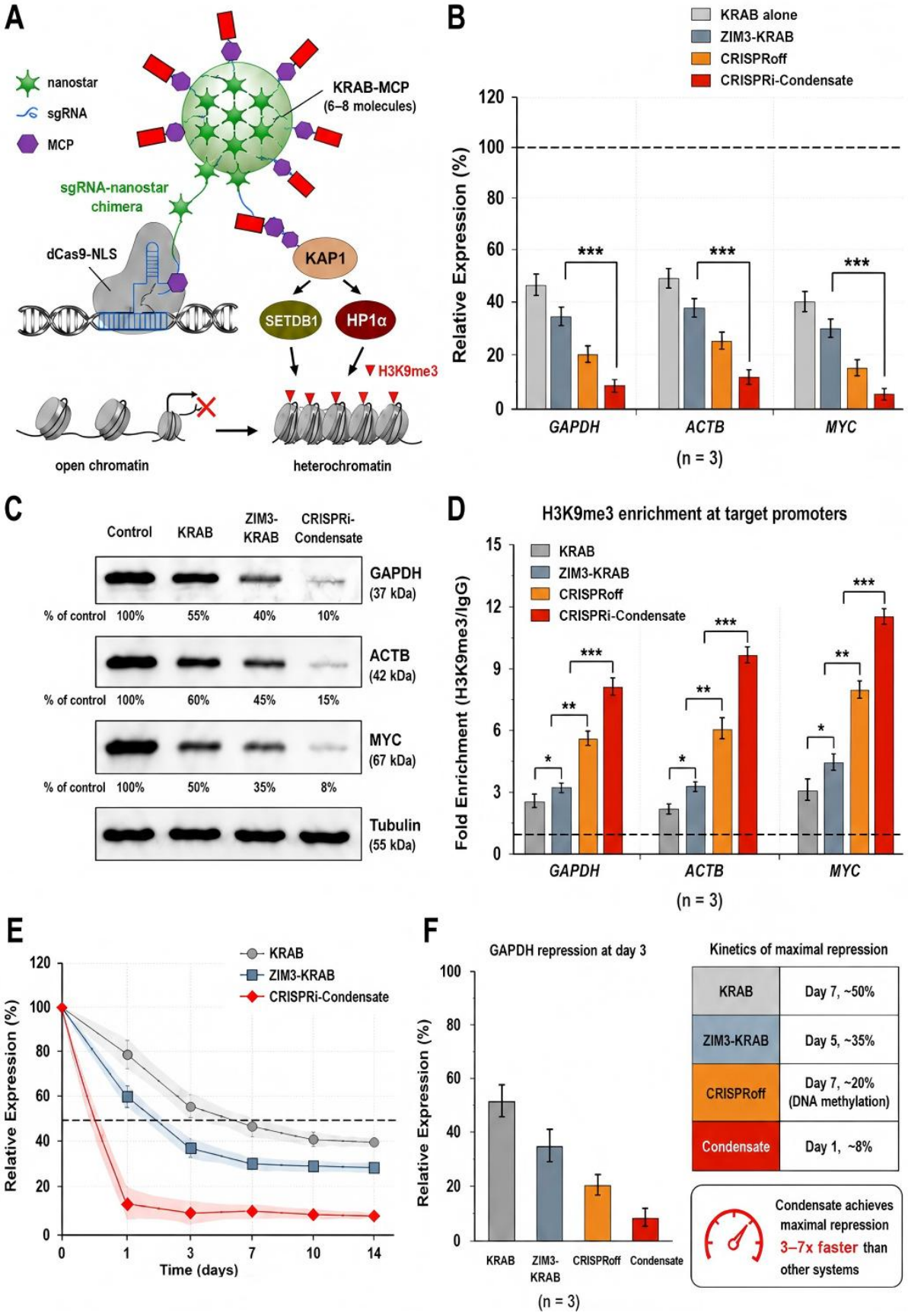
A
nanostar
sgRNA
MCP
KRAB-MCP
(6–8 molecules)
sgRNA-nanostar
chimera
dCas9-NLS
KAP1
SETDB1
HP1α
H3K9me3
open chromatin
heterochromatin
B
KRAB alone
ZIM3-KRAB
CRISPRoff
CRISPRi-Condensate
Relative Expression (%)
120
100
80
60
40
20
0
***
***
***
GAPDH
ACTB
MYC
(n = 3)
C
Control
KRAB
ZIM3-KRAB
CRISPRi-Condensate
GAPDH
(37 kDa)
% of control 100% 55% 40% 10%
ACTB
(42 kDa)
% of control 100% 60% 45% 15%
MYC
(67 kDa)
% of control 100% 50% 35% 8%
Tubulin
(55 kDa)
D
H3K9me3 enrichment at target promoters
KRAB
ZIM3-KRAB
CRISPRoff
CRISPRi-Condensate
Fold Enrichment (H3K9me3/IgG)
15
12
9
6
3
0
GAPDH
ACTB
MYC
(n = 3)
E
KRAB
ZIM3-KRAB
CRISPRi-Condensate
Relative Expression (%)
120
100
80
60
40
20
0
0
1
3
7
10
14
Time (days)
F
GAPDH repression at day 3
Relative Expression (%)
100
80
60
40
20
0
KRAB
ZIM3-KRAB
CRISPRoff
Condensate
(n = 3)
Kinetics of maximal repression
KRAB
Day 7, ~50%
ZIM3-KRAB
Day 5, ~35%
CRISPRoff
Day 7, ~20%
(DNA methylation)
Condensate
Day 1, ~8%
Condensate achieves
maximal repression
3–7x faster than
other systems

Figure 3: CRISPR-Condensate enables robust and durable transcriptional repression.

A, Illustration of CRISPRi-Condensate. dCas9-NLS is tethered to the sgRNA-nanostar-MS2SL chimera at the target site, while KRAB-MCP is recruited to the nanostar condensate via MS2SL-MCP binding, which allows for local clustering of KRAB domains to drive the recruitment of KAP1, HP1 binding, and H3K9me3 deposition mediating the establishment of stable heterochromatin. B, RT-qPCR fold-repression at 3 endogenous loci (GAPDH, ACTB, MYC). CRISPRi-Condensate reduced residual target-gene expression to approximately 5–12% of control, corresponding to approximately 88–95% knockdown. Standard dCas9-KRAB left approximately 40–50% residual expression. GAPDH repression has been included as a demonstration of proof-of-concept efficacy against a heavily transcribed euchromatic housekeeping gene. Error bars = s.d., n = 3 biological replicates. C, Western blot showing protein reduction at the GAPDH target. CRISPRi-Condensate delivers 20–30-fold repression (95–98% knockdown) over KRAB-dCas9, CRISPRi-Condensate reduces GAPDH by 96% at the protein level. α-Tubulin is a loading control. Full western blot for all three targets (GAPDH, ACTB, MYC) and all KL variants are found in Figure S9. D, ChIP-qPCR of H3K9me3 at the GAPDH promoter: 12-fold for Condensate vs 3-fold for KRAB-dCas9. H3K9me3 spreading reaches up to 6 kb for Condensate vs ~1 kb for KRAB-dCas9. E, Representative long-term repression kinetics over two weeks of continuous culture without selection at the GAPDH locus. CRISPRi-Condensate sustains >90 % repression (95 % at day 2, 92 % at day 14) as opposed to decaying repression for KRAB-dCas9 (~75 % at day 2, ~60 % at day 14). F, Comparison of residual GAPDH expression at day 3 and the approximate time required to reach maximal repression. Data are mean ±s.d. n = 3 biological replicates.

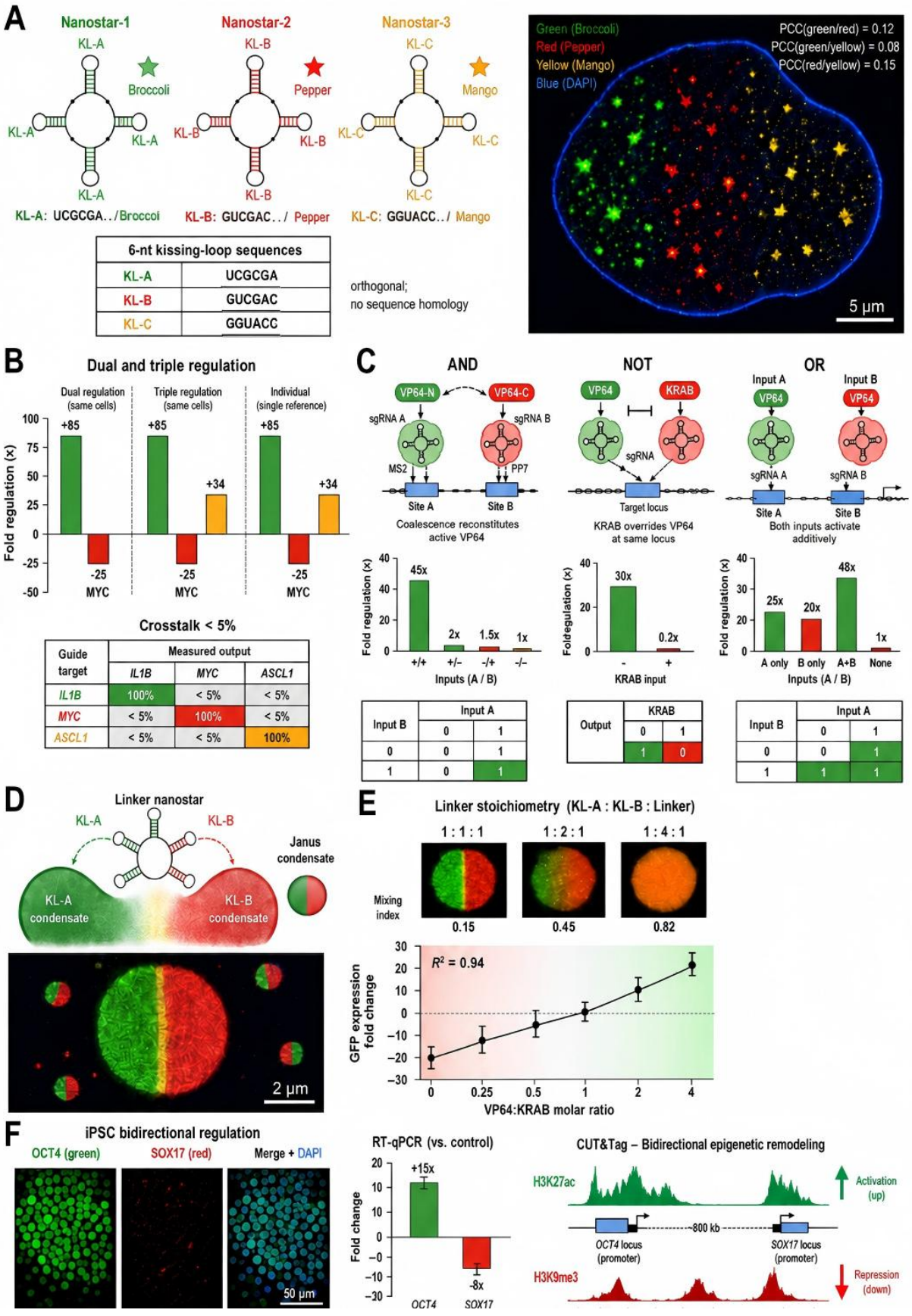
A
Nanostar-1
Nanostar-2
Nanostar-3
KL-A
KL-B
KL-C
Broccoli
Pepper
Mango
KL-A: UCGCGA../Broccoi
KL-B: GUCGAC../ Pepper
KL-C: GGUACC../ Mango
6-nt kissing-loop sequences
KL-A UCGCGA
KL-B GUCGAC
KL-C GGUACC
orthogonal;
no sequence homology
Green (Broccoli)
Red (Pepper)
Yellow (Mango)
Blue (DAPI)
PCC(green/red) = 0.12
PCC(green/yellow) = 0.08
PCC(red/yellow) = 0.15
5 µm
B
Dual and triple regulation
Dual regulation (same cells)
Triple regulation (same cells)
Individual (single reference)
Fold regulation (x)
+85
+34
-25
MYC
Crosstalk < 5%
Guide target
Measured output
IL1B
MYC
ASCL1
100%
< 5%
C
AND
NOT
OR
VP64-N
VP64-C
sgRNA A
sgRNA B
MS2
PP7
Site A
Site B
Coalescence reconstitutes active VP64
VP64
KRAB
sgRNA
Target locus
KRAB overrides VP64 at same locus
Input A
Input B
Both inputs activate additively
45x
2x
1.5x
1x
Inputs (A / B)
30x
0.2x
KRAB input
25x
20x
48x
A only
B only
A+B
None
Output
D
Linker nanostar
KL-A
KL-B
Janus condensate
KL-A condensate
KL-B condensate
2 µm
E
Linker stoichiometry (KL-A : KL-B : Linker)
1 : 1 : 1
1 : 2 : 1
1 : 4 : 1
Mixing index
0.15
0.45
0.82
R^2 = 0.94
GFP expression fold change
VP64:KRAB molar ratio
F
iPSC bidirectional regulation
OCT4 (green)
SOX17 (red)
Merge + DAPI
50 µm
RT-qPCR (vs. control)
+15x
-8x
OCT4
SOX17
CUT&Tag – Bidirectional epigenetic remodeling
H3K27ac
Activation (up)
800 kb
OCT4 locus (promoter)
SOX17 locus (promoter)
H3K9me3
Repression (down)

Figure 4: Multiplexed gene regulation via orthogonal and sub-compartmentalized condensates.

A, Orthogonal KL designs. There are three types of nanostar, each with a unique KL sequence, such as KL-A (Broccoli/ green), KL-B (Pepper/ red) and KL-C (Mango/ yellow). These nanostars give rise to condensate populations that do not mix. Use KL-A = UCGCGA, KL-B = GUCGAC, KL-C = GGUACC; PCC = 0.12, 0.08, and 0.15. Broccoli / Pepper = 0.08, Broccoli / Mango = 0.05, Pepper / Mango = 0.11. Scale bar, 5 μm. B, Simultaneous activation and repression. sgRNA-KL-A + VP64 activates IL1B (85-fold); sgRNA-KL-B + KRAB represses MYC (25-fold). Three-color regulation adds ASCL1 activation (34-fold) with minimal crosstalk (<5%) (<1.3-fold). C, Logic gates. AND gate: Reconstituted VP64 induced 45-fold activation only when both inputs were present. NOT gate: KRAB repression and VP64 activation at the same promoter reduced output from approximately 30-fold to 0.2-fold. OR gate: additive activation of approximately 48-fold combined. Truth tables for each gate are shown. D, Janus condensates. RNA linker nanostars form hemispherical sub-compartmentalized structures by bridging KL-A/VP64 and KL-B/KRAB condensates. Scale bar has a length of 2 micrometers. 1:1:1 ratio produces sharp Janus (JR = 0.18); 1:4:1 produces complete mixing (JR = 0.85). VP64-MCP:KRAB-MCP molar ratio yields linear GFP output (R^2 = 0.94). E, Janus condensate stoichiometry and mixing index. The mixing index increased from 0.15 at 1:1:1 to 0.45 at 1:2:1 and 0.82 at 1:4:1. Titration of the VP64-MCP:KRAB-MCP molar ratio yields a linear relationship with GFP reporter expression (R^2 = 0.94). Mixing indices for all pairwise KL variant combinations, together with representative images of demixed versus co-mixed condensates, are shown in Figure S12. F, iPSC bidirectional regulation. OCT4 was induced 15-fold, while SOX17 was repressed 8-fold. CUT&Tag displays the increased H3K27ac enrichment at the OCT4 promoter and increased H3K9me3 enrichment at the SOX17 promoter, consistent with simultaneous locus-specific activation and repression H3K27ac and H3K9me3. These marks are separated by 0.5 ± 0.2 μm. Scale bar, 50 μm. Data represent the mean±s.d. for N = 3 biological replicates.

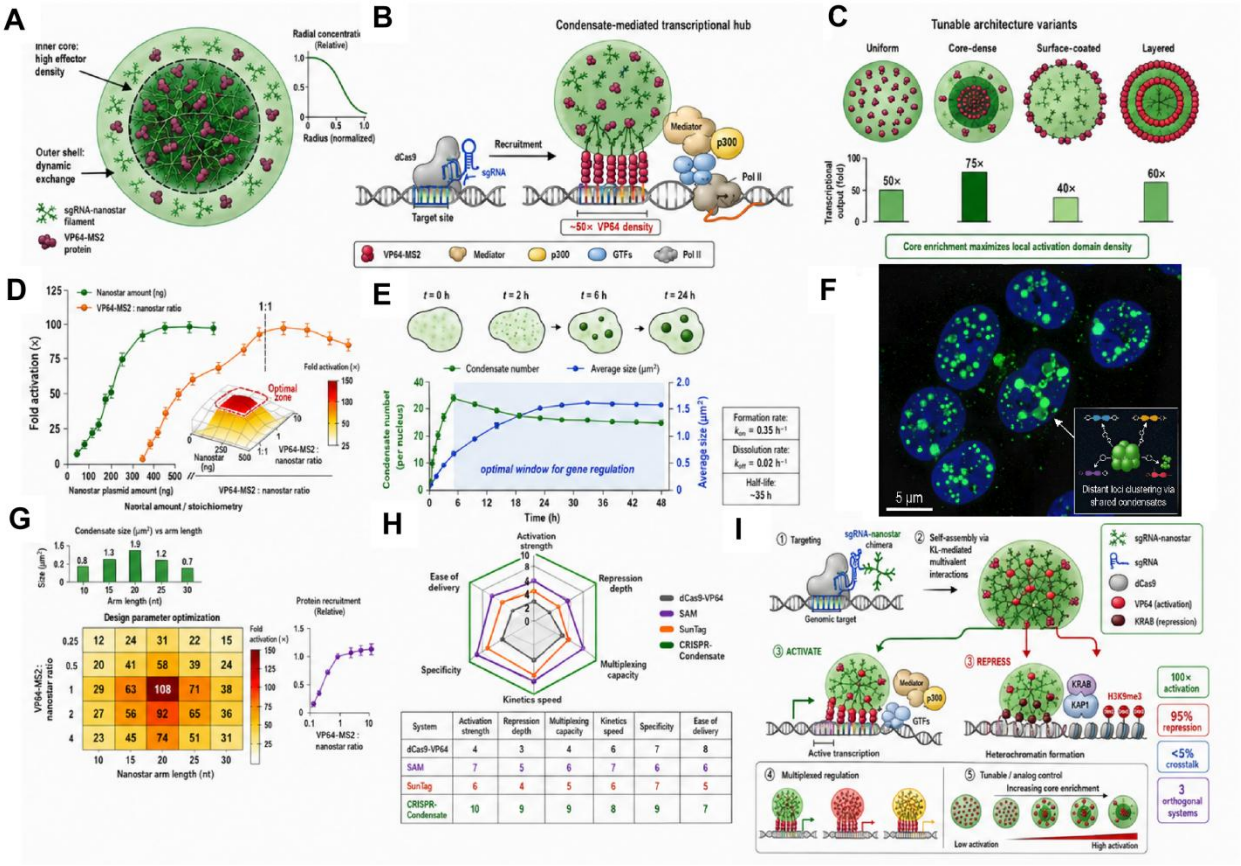

Figure 5: Model overviews and optimization of design parameters

A, Core-shell condensate architecture showing inner core (high effector density, dark green) and outer shell (dynamic exchange, light green). B, Recruitment model: nanostar condensate docks at DNA target via dCas9, concentrating VP64 domains to recruit Pol II and transcription machinery. C, Tunable architecture variants: uniform, core-dense, surface-coated, and layered configurations with corresponding transcriptional outputs (core-dense = 75× highest). D, Dose-response titration showing optimal nanostar-to-effector stoichiometry at 1:1. E, Spatiotemporal dynamics of condensate formation: condensate number peaks at ~6 h and size plateaus at ~24 h. F, Multi-condensate clustering enabling combinatorial regulation of distant loci. G, Composition-function heatmap showing gene activation as a function of nanostar arm length and VP64-MCP:sgRNA-NS(MS2SL) ratio; optimal zone at 20-nt arms with 1:1 ratio. H, Radar plot comparison of CRISPR-Condensate (green) to VP64 (grey), SAM (purple), and SunTag (orange) in six categories: activation potential, repression depth, multiplexing ability, kinetics, specificity, and delivery. I, Working model: sgRNA-nanostar chimeras nucleate phase-separated condensates at target loci, concentrating effector molecules for robust activation or repression; orthogonal systems support multiplexed modulation; Janus architecture supports bidirectional regulation. Data are mean±s.d. from n = 3 biological replications.